International Journal of Multiphase Flow 181 (2024) 105004

Contents lists available at ScienceDirect

International Journal of Multiphase Flow

journal homepage: www.elsevier.com/locate/ijmulflow

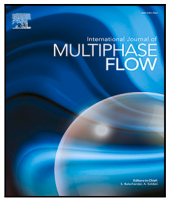

Morphology and dynamics of the liquid jet in high-speed gas-assisted atomization retrieved through synchrotron-based high-speed X-ray imaging

Oliver Tolfts [a], Alexander Rack [b], Nathanaël Machicoane [a,*]

[a] Univ. Grenoble Alpes, CNRS, Grenoble INP, LEGI, 38000 Grenoble, France
[b] ESRF - The European Synchrotron, 38000 Grenoble, France

ARTICLE INFO

Keywords:
Atomization
Coaxial two-fluid atomizer
High-speed spray
Fragmentation
Synchrotron-based high-speed X-ray imaging

ABSTRACT

The breakup of a liquid jet by a surrounding high-speed gas jet with different liquid Reynolds numbers and gas Weber numbers was studied using high speed phase-contrast X-ray imaging technique. Focusing on the liquid core, the portion of liquid that is connected to the nozzle, four distinct morphologies were observed and can be associated with changes in the large-scale configurations of the two-phase flow are reported in a phase diagram. Gas-to-liquid kinetic energy balance arguments capture several transitions between the liquid core regimes. The temporal evolution of the center of mass of the liquid core is extracted to quantify its motion, whose statistics can be utilized as a signature to distinguish different regimes. At low to moderate gas Weber numbers, the dynamics are strongly influenced by flapping, while long-time dynamics develop at high Weber numbers, that give way to quasi-periodic motions when swirl is impeded to the gas jet.

1. Introduction

Gas-assisted atomization, *i.e.,* the fragmentation of a liquid jet by a gas jet is a complex process where the aerodynamic stresses prevail on the liquid surface tension force (whose ratio forms the gas Weber number) to break the liquid into a spray (Lasheras and Hopfinger, 2000; Villermaux, 2020). At moderate Weber numbers, a good understanding of the atomization mechanisms, for instance, interfacial instabilities (Fuster et al., 2013; Matas et al., 2018; Ling et al., 2019; Singh et al., 2020), led to a certain level of predictive capability (*e.g.,* Jackiw and Ashgriz, 2023). In opposition, high Weber number gas-assisted atomization is a process which, while largely used in propulsion applications (*e.g.,* rocket engines), is still impossible to model reliably given its complexity, impacting safety issues and pollutant emission. Studying such phenomena can be done using cryogenic benches at the expense of high running costs and strong technical constraints. The strategy proposed here is to target very high gas velocities instead. When studying the atomization of a liquid jet by a high-speed gas jet, the resulting turbulent two-phase flow cannot be probed accurately using visible light as it becomes optically dense. X-ray, unlike visible light, suffers from only weak scattering by gas–liquid interfaces and is particularly suited to probe such two-phase flows (Aliseda and Heindel, 2021), due to its penetrative nature and high energy. This is particularly true when using Synchrotron X-ray sources (Powell et al., 2000; Cai et al., 2003). The focus of this work, conducted in the context of diesel sprays, was on the liquid mass distributions in the near-field, which was retrieved by using a focused monochromatic X-ray beam (half a dozen μm across) and measuring absorption along that line-of-sight with a diode. Shortly after, Wang et al. (2008) imaged coaxial atomization using X-ray for the first time and showed ligament breakup around a liquid jet by a high-speed gas flow. This was achieved using a broader and polychromatic X-ray beam (half a dozen mm across[1]). The X-ray beam is absorbed by a scintillator crystal, that reemits visible light that can be captured by a camera, and either single independent snapshots were captured, or the superposition of a few snapshots on the same image (multi-exposure), due to camera limitations.

More recently, Machicoane et al. (2019) were able to perform time-resolved imaging of the atomization process of a coaxial gas-assisted atomizer using the same approach but taking advantage of the advances of modern high-speed cameras to study the morphology of the liquid core (portion of the liquid jet hydraulically connected to the nozzle). A gas recirculation behind the liquid core was directly imaged for the first time: ligaments are pulled from the periphery of a hollowed-out liquid core (the "crenelations" terming this morphology as a liquid

* Corresponding author.
E-mail address: nathanael.machicoane@univ-grenoble-alpes.fr (N. Machicoane).

[1] The increase in cross-section requires more energy which is attained by letting the full spectrum of the Synchrotron-produced X-ray at APS-ANL, while previous work filtered it to a narrow bandwidth. More detail about both techniques can be found in Kastengren et al. (2010, 2012), Bothell et al. (2020), Li et al. (2019).

https://doi.org/10.1016/j.ijmultiphaseflow.2024.105004
Received 10 August 2024; Received in revised form 19 September 2024; Accepted 19 September 2024
Available online 26 September 2024

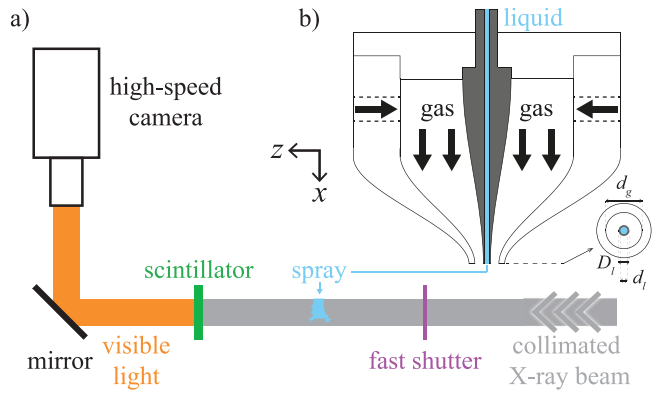

Fig. 1. Experimental setup with X-ray imaging configuration (a) and coaxial two-fluid atomizer (b).

crown). The crown is found at high values of the gas-to-liquid dynamic pressure ratio M, while no gas penetration is found for lower M (which is referred to as intact core). When gas swirl is employed at high M, the gas recirculation is able to penetrate inside the liquid nozzle, and the liquid can only exit through a reduced cross-section. Similarly to the recirculation behind a blunt body (Grandemange et al., 2013), the gas recirculation is unstable and switches position within the liquid nozzle cross-section, driving the motion of the liquid crown (hence termed unstable crown). Following this work, high-speed spray formation is studied over long recordings using a quasi-monochromatic X-ray beam (Section 2), establishing a phase diagram of the liquid core morphology in a broad and tightly sampled parameter space (Section 3). The dynamics of the liquid core center of mass are studied to quantitatively establish change in regime in Section 4, followed by a discussion and conclusions (Section 5).

2. Experimental setup and measurements

The coaxial two-fluid atomizer described in Machicoane et al. (2019), Tolfts et al. (2023) is used for this study (Fig. 1). Water is injected through a 100-mm long pipe, reaching a fully developed flow. The mean exit velocity U_l is varied to change the liquid Reynolds number $Re_l = U_l d_l \nu_l$ in the range $780 \leq Re_l \leq 4400$, with $d_l = 1.89$ mm the liquid nozzle inner diameter and ν_l the kinematic viscosity of water. The liquid nozzle is centered in a gas nozzle, where air is injected through 4 ports, and exits through an annular cross-section of area $A_g = \pi(d_g^2 - D_l^2)/4$, where $D_l = 3.1$ mm is the inner diameter and $d_g = 9.985$ mm the outer diameter. Four additional ports, placed off-axis with respect to the nozzle, can be used to impede angular momentum (swirl) to the gas flow. Swirl is characterized by the ratio of the flow rate of those ports Q_{SW} to the one of the on-axis ports Q_{NS} as $SR = Q_{SW}/Q_{NS}$, that can be varied while keeping the total gas flow rate $Q_g = Q_{SW} + Q_{NS}$ constant. The gas volumetric flow rate exiting the nozzle Q_g is used to define a gas mean exit velocity and a gas Reynolds number, as $U_g = Q_g/A_g$ and $Re_g = 4Q_g/\sqrt{4\pi A_g}\nu_g$, where ν_g is the kinematic viscosity of air. In addition, results will be reported in terms of the gas-to-liquid dynamic pressure ratio $M = \rho_g U_g^2/\rho_l U_l^2$ and the gas Weber number based on the liquid jet $We_g = \rho_g U_g^2 d_l/\sigma$. Table 1 provides reference values of the non-dimensional parameters that are representative of the study.

The dynamics of the liquid core are imaged using high-speed phase-contrast X-ray imaging at beamline ID19 of the European Synchrotron Radiation Facility (ESRF) to tackle the optical density of the turbulent two-phase flow at the exit of the atomizer at high gas Weber numbers (Fig. 1). A collimated X-ray beam, with over 85% of its energy contained at 18.2 keV, passes through the liquid jet, and its intensity, converted into visible light by a scintillator crystal, is recorded by a high-speed camera. Due to the finite size of the beam diameter, an imaging window of 6.86 mm and a spatial resolution of 6.7 μm is chosen, and recordings of 1 s (limited by the heat load to the scintillator crystal) between 10 and 50 kHz are taken.

Table 1
Flow parameters for a given liquid injection ($U_l = 0.42$ m/s, $Re_l = 780$), varying the total gas flow rate Q_g. The gas velocity is $U_g = Q_g/A_g$, the gas Reynolds number is $Re_g = 4Q_g/\sqrt{4\pi A_g}\nu_g$, the gas-to-liquid dynamic pressure ratio is $M = \rho_g U_g^2/\rho_l U_l^2$, and the gas Weber number is based on the liquid diameter as $We_g = \rho_g U_g^2 d_l/\sigma$. The fluids are air and distilled water, at an ambient temperature of 20 °C, with kinematic viscosities of $\nu_g = 1.52\ 10^{-5}$ m^2 s^{-1} and $\nu_l = 1\ 10^{-6}$ m^2 s^{-1}, densities $\rho_g = 1.2$ kg m^{-3} and $\rho_l = 998$ kg m^{-3}, and the air–water surface tension $\sigma = 71$ mN m^{-1}. The liquid core morphologies are defined in Section 3. This represents a subset of the conditions as the liquid injection rate is varied up to reaching a liquid Reynolds number of $Re_l = 4400$, with $U_l = 2.35$ m/s, while keeping the dynamic pressure ratio above 6 (up to the maximal value reached of 670, with $U_l = 0.42$ m/s and $U_g = 318$ m/s) to ensure a short enough liquid core.

U_g (m/s)	Re_g	M	We_g	Morphology
42	26 080	11.9	56	Intact core
82	51 490	44.6	217	Transitional
112	70 560	83.8	407	Crown
189	118 360	274	1146	Unstable crown

The X-ray images result from the combination of an absorption signal, following the Beer–Lambert law relating it to the traversed medium depth and its refractive index (*i.e.,* integrated along the beam), and interference patterns originated by the weak scattering of the incoming collimated X-ray beam on curved interfaces. With the object-to-detector distance of 4 m used here and the pixel size of 6.7 μm, the interferences only occupy a few pixels and are used to highlight the gas–liquid interfaces. Without scattering, many interfaces would not be visible, especially for small liquid structures (*e.g.,* ligaments, films, encapsulated air bubbles) that do not result in a strong absorption signal. When a direct relation between the detected signal and the liquid mass density is needed, for instance, to compute equivalent path length (EPL) maps (more details in Tolfts (2023)), ANKAphase (Weitkamp et al., 2011) is used, which calculates from a fringe-dominated X-ray phase contrast image the value of the phase shift a wavefront locally undergoes when transmitting the sample (Paganin et al., 2002).

3. Regimes of the liquid core morphology

The high-speed phase-contrast X-ray imaging, highlighting the gas–liquid interfaces, allows for the determination of the liquid core with no ambiguity, even at very high values of the gas Weber number, and its morphology can be studied in detail (Fig. 2). In agreement with previous work (Machicoane et al., 2019), the intact core observed at low Weber numbers (see for instance video at $U_l = 0.42$ m/s, $U_g = 42$ m/s, *i.e.,* $Re_l = 780$, $We_g = 56$, and $M = 12$ in the Supplementary material), where no gas recirculation is found within the liquid core, gives way to a liquid crown at higher gas Weber numbers, with a large-scale recirculation located immediately downstream of a short liquid core (see for instance video at $U_l = 0.59$ m/s, $U_g = 163$ m/s, *i.e.,* $Re_l = 1120$, $We_g = 847$, and $M = 90$ in the Supplementary material). However, the tight sampling of the parameter space and the explorations of a range of liquid injection rates highlight a transition regime between intact core and crown (Fig. 3). At low to moderate liquid Reynolds numbers, the gas recirculation is unstable in time and the liquid core can alternate between intact and crown. At higher liquid Reynolds numbers, this transitional regime takes another form, with many small-scale gas recirculations of short lifetimes, that perforate the liquid core (see for instance video at $U_l = 1.7$ m/s, $U_g = 163$ m/s, *i.e.,* $Re_l = 3120$, $We_g = 847$, and $M = 12$ in the Supplementary material). Many overlapping gas–liquid interfaces are observed in this highly dynamic regime, with a large number of encapsulated air bubbles that result in the folding of the gas–liquid interface on itself caused by the small recirculations in addition to the localized instabilities.

In addition to the new transitional regime, varying the liquid Reynolds number range can yield extremely high values of the gas-to-liquid dynamic pressure ratio, where an unstable crown regime is observed (see for instance video at $U_l = 0.42$ m/s, $U_g = 188$ m/s,

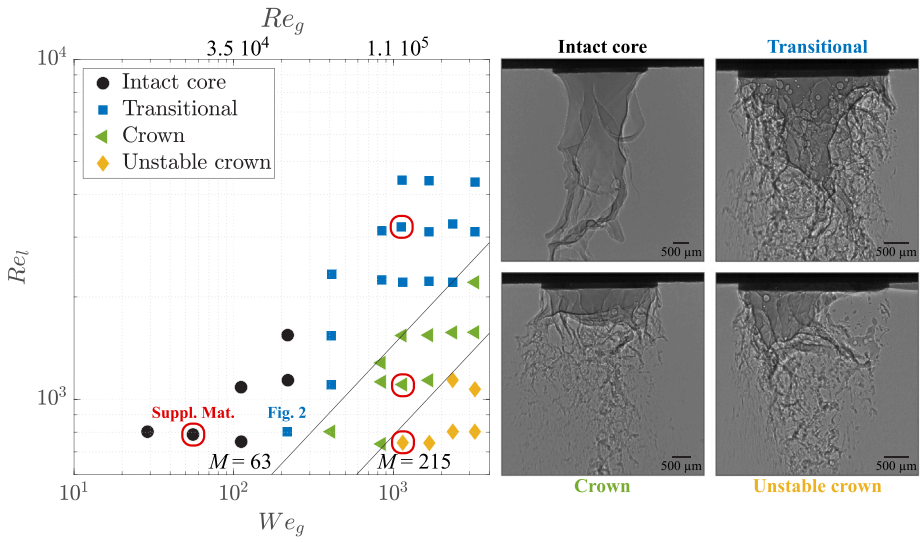

Fig. 2. Phase diagram of the morphology of the liquid core in the liquid Reynolds number Re_l, gas Weber number We_g parameter space, with example pictures of the four identified morphologies. The gas Reynolds number Re_g is indicated on the top axis, and iso-values of the gas-to-liquid dynamic pressure ratio $M = 63$ and 215 are displayed. Movies of the conditions highlighted in red can be found in the Supplementary Materials. (For interpretation of the references to color in this figure legend, the reader is referred to the web version of this article.)

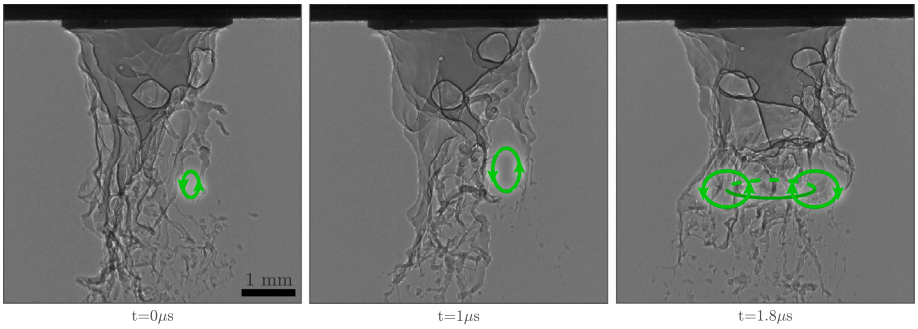

Fig. 3. Radiographs of the atomization process at the exit of the nozzle at $Re_l = 780$ and $We_g = 218$ presenting a liquid core morphology in the transitional regime between intact core and crown with gas recirculations indicated by arrows.

i.e., $Re_l = 780$, $We_g = 1138$, and $M = 248$ in the Supplementary material). This stands as the first observation of this regime in the absence of gas swirl (which was only previously attained for $SR \geq 0.5$ (Machicoane et al., 2019)). Finally, while the transition between intact core and the transitional regime is unclear with the sampled conditions, the subsequent transitions to crown and unstable crown appear to be in good agreement with iso-M lines of values $M = 63$ and 215 (Fig. 2).

4. Dynamics of the liquid core

The EPL maps are used to compute the time series of the center of mass of the liquid jet. Since liquid mass is already integrated along the beam direction (z) by the X-ray projection onto the sensor, the transverse motion of the liquid jet is analyzed by studying the center of mass along y, $Y_M(t)$, taken at $x = d_l/2$ for simplicity. This means that the azimuthal motions are perceived as in-plane left–right motions. Fig. 4 presents the time series and associated probability density functions. A condition per morphology was chosen to represent its dynamics, at increasing gas Weber number and for a fixed value of the liquid Reynolds number $Re_l = 780$. In addition, a condition with azimuthal momentum in the gas jet (swirl) is included, with $SR = 0.8$ and the other parameters kept constant, to discuss the effect of swirl on the motions of the unstable crown.

The time series and PDF appear roughly similar for the intact core, transitional, and crown regime. While the fluctuations seem to happen on faster timescales as We_g increases, their levels are the highest in the transitional regimes ($Y'_M = 0.026R_l$, versus approximately $0.02R_l$ for the two other cases). This may be due to the transitional nature of the regime where the morphology of the liquid core strongly varies in time, unlike the crown that is stabilized by the large-scale gas recirculation, and the intact core that remains only weakly perturbed in the vicinity of the nozzle's exit plane. Another explanation comes from the flapping of the liquid jet, which bears a clear signature on the motion of the liquid core (the temporal dynamics is discussed below, see Fig. 5), which, while its amplitude decreases with decreasing liquid core length (Kaczmarek et al., 2022), plays a large role in the fluctuations of Y_M. Conditions in the intact core and crown regime are characterized by $M \leq 63$ and hence present longer liquid core lengths (Machicoane et al., 2020, 2023; Tolfts et al., 2023). However, those variations are much smaller than the large deviations of the center of mass found in the unstable crown regime ($Y'_M = 0.056R_l$ without swirl, and $0.058R_l$ for a swirled unstable crown), whose bimodal PDF stands as a clear quantitative signature of this regime. Once again note that this left–right bimodal shape in this axisymmetric configuration, where the unstable crown is anchored along a portion of the liquid nozzle and moves along its circumference, is only caused by the projection along the beam direction, and highlights the fact that the center of mass is almost never centered on the nozzle's axis (low probability of having $Y_M = 0$, which is the situation created by the three other morphologies, where the jet is anchored along the whole periphery of the liquid nozzle). That shape can simply be modeled by geometrical arguments (Tolfts, 2023), and the lack of symmetry here is due to a lack of data convergence. The difficulty in retaining symmetries in

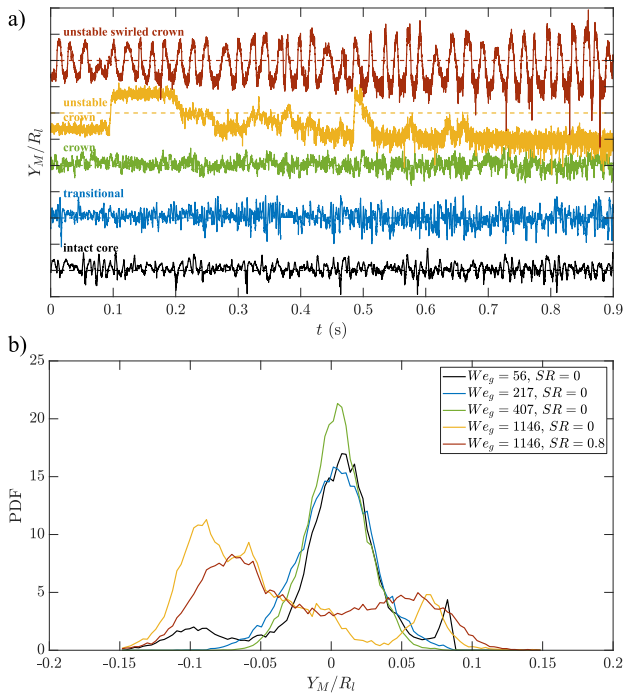

Fig. 4. Time series (a) and probability density functions (b) of the center of mass of the liquid jet along y, normalized by the liquid nozzle outer radius, Y_M/R_l. The liquid Reynolds number is kept constant at $Re_l = 780$ and the gas Weber numbers is increased from $We_g = 56$ to 1146 to span the four morphologies of the liquid core. At the highest value, a condition with the same total gas flow rate, but with swirl in the gas jet at $SR = 0.8$ is also considered. The time series (a) are successively shifted by $0.2R_l$, but the ranges of variations of Y_M is visible in the PDF (b).

the experimental measurements of such multistable systems is a well-documented challenge, that is very common in the general contexts of physics, chemistry, or biology (Kramers, 1940; Van Kampen, 1981), and has been many times reported in fluid mechanics with fluctuation-driven bi-stable systems (*e.g.,* Constable, 2000; Benzi, 2005; Berhanu et al., 2007; de la Torre and Burguete, 2007; Grandemange et al., 2013 as well as other multiphase flows, Maxey (1987), Djeridi et al. (1999), Climent et al. (2007), Machicoane et al. (2016), Machicoane and Volk (2021), Stamati et al. (2023)).

The changes highlighted here on the statistics of the liquid core center of mass through transitions in its morphology are also visible in its temporal dynamics. Fig. 5 presents the auto-correlation functions and power spectral densities (PSD) of Y_M. In the intact core and transitional regime, flapping dominates the temporal dynamics, marked by oscillations of the auto-correlation functions and a peak on the power spectra, located within the plateau found in the low-to-moderate frequency. In the crown regime, flapping remains noticeable but is much weaker, since the flapping frequency is found within the high-frequency power-law decay that corresponds to the small-scale fluctuations. This corresponds to a trough and hump feature in the decay of the auto-correlation function. In the unstable crown regime, the erratic motion of the liquid core along the nozzle's circumference results in the emergence of long-time dynamics, highlighted by the power law (exponent -1.6) found in the low-frequency range. This results in an auto-correlation function that retains correlated dynamics over very long times. The slight change of slope of R_{Y_M} at short times (around 15 ms) highlights the small difference in scaling in the low and high-frequency range that is less noticeable on the PSD. The long-time dynamics of the unstable crown regime would require much longer acquisition to be further investigated, with for instance the extraction of residence times and their distributions.

The peak that corresponds to the flapping of the liquid jet is reported along the gas velocity in Fig. 5(d) in a non-dimensional way, with error bars associated with the frequency resolution for the first three points (up to the crown regime). The points for the two highest velocities are in the unstable crown regime (PSD not shown here for $U_g = 271$ m/s, corresponding to $We_g = 1950$), conditions where the flapping peak falls within the high-frequency range and associating a unique frequency become more challenging, so the width of the peak is given as error bars. The flapping frequency is also extracted from the oscillation period of the auto-correlation functions, only measurable for the first 3 points, which, as expected, agrees well with the frequencies from the PSD. Unlike the linear relationship $f \propto U_g$ proposed by Delon et al. (2018), a steeper growth is reported, resulting in a Strouhal number $St = f d_g/U_g$ linearly increasing with Re_g.

When swirl is added to the gas jet, a strong periodicity is observed on the time series, which results in oscillations of the auto-correlation functions and a broad peak at low-frequency, centered around $f_{peak} = 49$ Hz. No signature of long-time dynamics is present, and this is confirmed by the auto-correlation functions, whose envelop follows a much faster decay than the one observed in the absence of gas swirl. This can be characterized by fitting R_{Y_M} by the function $\cos(t/2\pi f_{fit})\mathrm{e}^{-t/\tau_{fit}}$, which yield $f_{fit} = 47$ Hz and $\tau_{fit} = 30$ ms ($\pm\mathrm{e}^{-t/\tau_{fit}}$ is represented by dashed lines in Fig. 5a), while the first zero-crossing happens around 5 ms. While the statistics of the motion of the liquid core are similar, drastic differences are observed in the temporal dynamics of the unstable crown (long-time dynamics) and swirled unstable crown (quasi-periodicity).

5. Discussion and conclusions

Thanks to a tight sampling of the parameter space, a phase diagram of the morphology of the liquid core in the (Re_l, We_g) parameter space was established with:

- The intact core regime, characterized by an intact central bulk whose surface is destabilized by ligaments and sheets of liquid (the term intact is used to express the fact that no gas recirculation is penetrating within the liquid core).
- The crown regime, where the liquid core is hollowed out by a large gas recirculation and ligaments are stripped off the edge of the liquid core.
- The transitional state between the intact core and the crown regime, where many small gas recirculations are observed in the liquid core.
- The unstable crown regime where the gas recirculation penetrates the liquid nozzle and pushes the liquid crown to a smaller region of the liquid nozzle (exiting through a smaller cross-section).

This showed for the first time that the unstable crown regime was reached for high values of M, without adding swirl in the gas jet, and demonstrated the existence of a transitional regime, occupying a wide region of the parameter space, between the intact core and crown regime. The previous study of Machicoane et al. (2019) only reported unstable crowns for conditions with gas swirl, since the slightly higher liquid Reynolds number value prevented to reach higher M values at a similar gas Weber number, and missed the transitional regime since only four values of the gas Weber number were explored (the focus being on swirl addition).

Considering a simple kinetic energy balance argument, the gas-to-liquid dynamic pressure ratio can be expected to capture the transitions between liquid core morphologies. This was empirically verified on the phase diagram and successfully described the transitions from transitional to crown regimes ($M > 63$) and from crown to unstable crown regimes ($M > 215$). While this argument should still hold for the transition between the intact core and the crown regimes, both regimes can be observed along iso-M lines (Fig. 2; two videos are provided at $M = 12$ in the Supplementary Material, one being in each regime), and a threshold value as $We_g \simeq 200$ may seem more appropriate (a more accurate threshold would require more conditions).

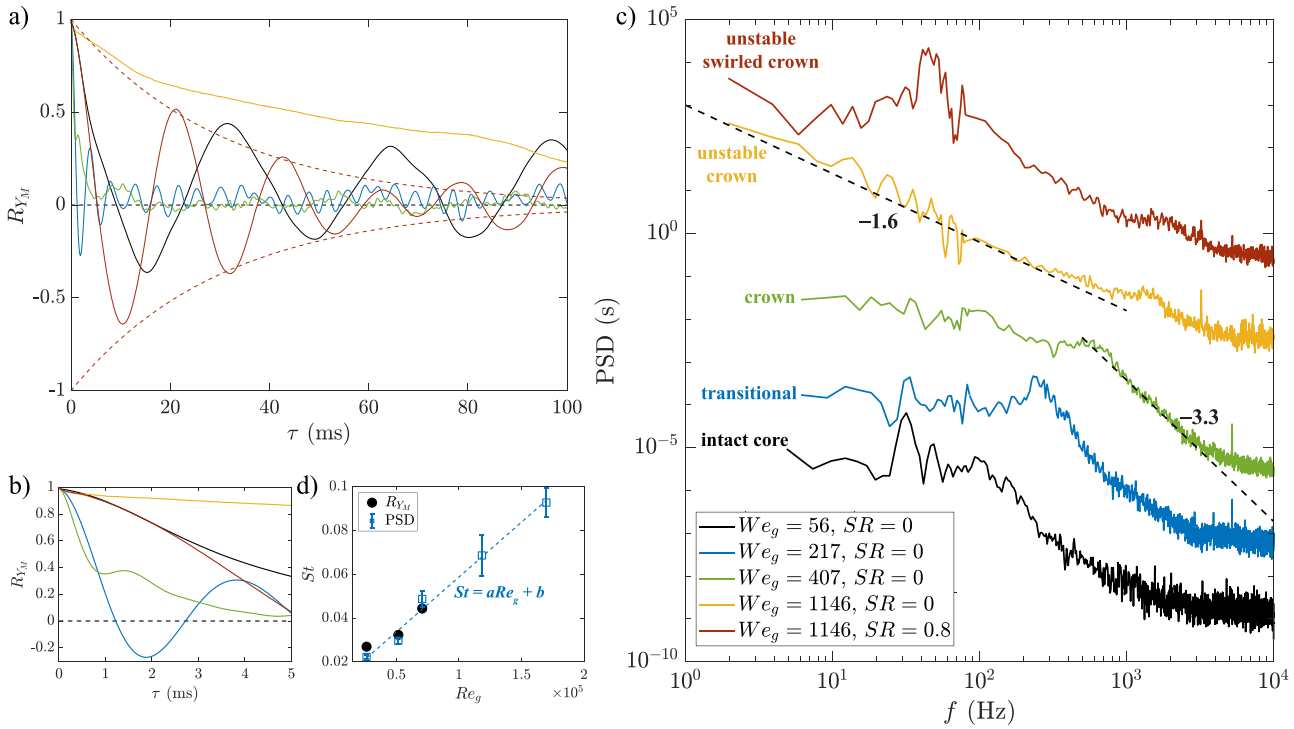

Fig. 5. Auto-correlation functions (a, with zoom in b) and power spectral densities (c) of the liquid jet's center of mass Y_M/R_l. The liquid Reynolds number is kept constant at $Re_l = 780$ and the gas Weber numbers is increased from $We_g = 56$ to 1146 to span the four morphology of the liquid core. At the highest value, a condition with the same total gas flow rate, but with swirl in the gas jet at $SR = 0.8$ is also considered. The PSD are successively shifted by a factor 100, and are computed in two parts using the Welch's method with two different sets of arguments to denoise the low and high-frequency range respectively. The dashed line in (a) is the envelope obtained by fitting the function $\cos(t/2\pi f_{fit})e^{-t/\tau_{fit}}$ for the swirled unstable crown case. (d) Flapping frequency extracted from the PSD or auto-correlation function, normalized as a Strouhal number: $St = f d_g/U_g$. The dashed line is a linear fit $St = aRe_g + b$ with $a = 5 \pm 1\ 10^{-7}$ and $b = 0.01 \pm 0.01$.

The motion of the liquid core was quantitatively extracted from the X-ray images, showing, in particular, the strong growth of the flapping frequency with gas velocity ($St \propto Re_g$) and long-time dynamics at high Weber numbers (Fig. 5). In addition to differences in the temporal features, the flow topology is assumed to change drastically around the primary breakup events between the different morphologies of the liquid jet, with a few proposed schematics sketched in Fig. 6. The well-documented case of co-flowing streams is expected to differ drastically from the case of a liquid crown due to the presence of gas recirculations that could result in strong gas velocity gradients around ligaments. In the case of an unstable crown, it is likely that, in addition to ligaments stretched by accelerating/curving flows, breakup in counterflows can occur as well (right part of Fig. 6c). In addition to changes in large-scale flow topology (from shear-driven instabilities, *e.g.,* (Marmottant and Villermaux, 2004; Ricard et al., 2021), to complex 3D structures responsible for breakup), the wetting dynamics at the nozzle exit, already of paramount importance in the intact core regime (Vu et al., 2023), may play a strong role for other morphologies. Furthermore, the presence of pockets of gas in the liquid jet (*e.g.,* Fig. 6b), whether bubbles within the bulk of the liquid jet or holes nucleated in thin liquid films, poses many questions on their origin(s) and consequences on spray formation as well as what parameters drive their presence and numbers. Investigating the potential analogy to the dynamics of hole nucleation in the two-phase planer mixing layer case (Ling et al., 2017) and how this relates to ligament formation in the crown regime appears of great interest. Furthermore, in the crown regime in particular, bubbles are observed to remain remarkably stable (having long lifetime and fluctuating around a stable position, without being advected downstream). This points towards the potential for recirculations being present within the liquid jet as well (Fig. 6b), as they would be able to entrap air bubbles in their core.

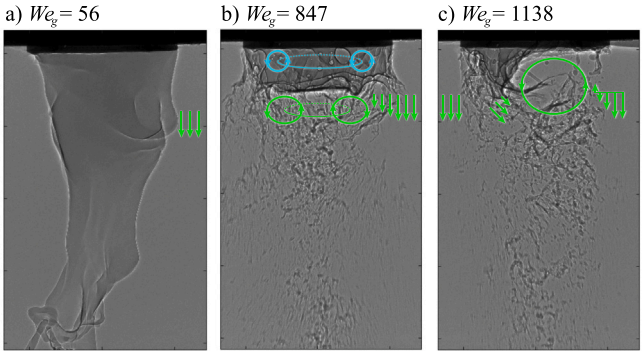

Fig. 6. Schematics of the expected gas flow topology around the breakup region for increasing gas Weber numbers in the intact core (a), crown (b), and unstable crown (c) regimes. The very stable bubbles observed in the crown regime are thought to be trapped in recirculating regions of the liquid jet that are also tentatively sketched.

CRediT authorship contribution statement

Oliver Tolfts: Visualization, Software, Methodology, Investigation, Formal analysis, Data curation, Conceptualization. **Alexander Rack:** Writing – review & editing, Software, Resources. **Nathanaël Machicoane:** Writing – review & editing, Writing – original draft, Validation, Supervision, Project administration, Methodology, Investigation, Funding acquisition, Formal analysis, Conceptualization.

Declaration of competing interest

The authors declare that they have no known competing financial interests or personal relationships that could have appeared to influence the work reported in this paper.

Data availability

Data will be made available on request.

Acknowledgments

This research was funded, in whole or in part, by the Agence Nationale de la Recherche under grant number ANR-22-CE30-0003-01. A CC-BY4.0 public copyright license has been applied by the authors to the present document and will be applied to all subsequent versions up to the Author Accepted Manuscript arising from this submission, in accordance with the grant's open access conditions. The European Synchrotron Radiation Facility (ESRF) is acknowledged for granting beamtime at beamline ID19 (proposal ME-1585).

Appendix A. Supplementary data

Supplementary material related to this article can be found online at https://doi.org/10.1016/j.ijmultiphaseflow.2024.105004.

References

Aliseda, A., Heindel, T.J., 2021. X-ray flow visualization in multiphase flows. Annu. Rev. Fluid Mech. 53, 543–567.
Benzi, R., 2005. Flow reversal in a simple dynamical model of turbulence. Phys. Rev. Lett. 95 (2), 024502.
Berhanu, M., Monchaux, R., Fauve, S., Mordant, N., Pétrélis, F., Chiffaudel, A., Daviaud, F., Dubrulle, B., Marié, L., Ravelet, F., Bourgoin, M., Odier, P., Pinton, J.-F., Volk, R., 2007. Magnetic field reversals in an experimental turbulent dynamo. Europhys. Lett. 77 (5), 59001.
Bothell, J.K., Machicoane, N., Li, D., Morgan, T.B., Aliseda, A., Kastengren, A.L., Heindel, T.J., 2020. Comparison of X-ray and optical measurements in the near-field of an optically dense coaxial air-assisted atomizer. Int. J. Multiph. Flow 103219.
Cai, W., Powell, C.F., Yue, Y., Narayanan, S., Wang, J., Tate, M.W., Renzi, M.J., Ercan, A., Fontes, E., Gruner, S.M., 2003. Quantitative analysis of highly transient fuel sprays by time-resolved x-radiography. Appl. Phys. Lett. 83 (8), 1671–1673.
Climent, E., Simonnet, M., Magnaudet, J., 2007. Preferential accumulation of bubbles in couette-taylor flow patterns. Phys. Fluids 19 (8).
Constable, C., 2000. On rates of occurrence of geomagnetic reversals. Phys. Earth Planet. Inter. 118, 181–193.
de la Torre, A., Burguete, J., 2007. Slow dynamics in a turbulent von Kármán swirling flow. Phys. Rev. Lett. (ISSN: 0031-9007) 99 (5), 3–6.
Delon, A., Cartellier, A., Matas, J.-P., 2018. Flapping instability of a liquid jet. Phys. Rev. Fluids 3 (4), 043901.
Djeridi, H., Fave, J.-F., Billard, J.-Y., Fruman, D., 1999. Bubble capture and migration in Couette–Taylor flow. Exp. Fluids 26 (3), 233–239.
Fuster, D., Matas, J.-P., Marty, S., Popinet, S., Hoepffner, J., Cartellier, A., Zaleski, S., 2013. Instability regimes in the primary breakup region of planar coflowing sheets. J. Fluid Mech. 736, 150–176.
Grandemange, M., Gohlke, M., Cadot, O., 2013. Turbulent wake past a three-dimensional blunt body. Part 1. Global modes and bi-stability. J. Fluid Mech. 722, 51–84.
Jackiw, I.M., Ashgriz, N., 2023. Aerodynamic droplet atomization model (ADAM). J. Fluid Mech. 958, A2.
Kaczmarek, M., Osuna-Orozco, R., Huck, P.D., Aliseda, A., Machicoane, N., 2022. Spatial characterization of the flapping instability of a laminar liquid jet fragmented by a swirled gas co-flow. Int. J. Multiph. Flow (ISSN: 0301-9322) 152, 104056.
Kastengren, A., Powell, C.F., Arms, D., Dufresne, E.M., Gibson, H., Wang, J., 2012. The 7BM beamline at the APS: a facility for time-resolved fluid dynamics measurements. J. Synchrotron Radiat. 19 (4), 654–657.
Kastengren, A.L., Powell, C.F., Arms, D., Dufresne, E.M., Wang, J., 2010. Spray diagnostics at the advanced photon source 7-bm beamline. In: ILASS Americas, 22nd Annual Conference on Liquid Atomization and Spray Systems, Cincinnati.
Kramers, H.A., 1940. Brownian motion in a field of force and the diffusion model of chemical reactions. Physica 7 (4), 284–304.
Lasheras, J.C., Hopfinger, E., 2000. Liquid jet instability and atomization in a coaxial gas stream. Annu. Rev. Fluid Mech. 32 (1), 275–308.
Li, D., Bothell, J.K., Morgan, T.B., Machicoane, N., Aliseda, A., Kastengren, A.L., Heindel, T.J., 2019. Time-averaged spray analysis in the near-field region using broadband and narrowband X-ray measurements. Atomiz. Sprays 29 (4).
Ling, Y., Fuster, D., Tryggvason, G., Zaleski, S., 2019. A two-phase mixing layer between parallel gas and liquid streams: multiphase turbulence statistics and influence of interfacial instability. J. Fluid Mech. 859, 268–307.
Ling, Y., Fuster, D., Zaleski, S., Tryggvason, G., 2017. Spray formation in a quasiplanar gas-liquid mixing layer at moderate density ratios: a numerical closeup. Phys. Rev. Fluids 2 (1), 014005.
Machicoane, N., Bothell, J.K., Li, D., Morgan, T.B., Heindel, T.J., Kastengren, A.L., Aliseda, A., 2019. Synchrotron radiography characterization of the liquid core dynamics in a canonical two-fluid coaxial atomizer. Int. J. Multiph. Flow (ISSN: 03019322) 115, 1–8.
Machicoane, N., López-Caballero, M., Fiabane, L., Pinton, J.-F., Bourgoin, M., Burguete, J., Volk, R., 2016. Stochastic dynamics of particles trapped in turbulent flows. Phys. Rev. E 93 (2), 023118.
Machicoane, N., Osuna-Orozco, R., Aliseda, A., 2023. Regimes of the length of a laminar liquid jet fragmented by a gas co-flow. Int. J. Multiph. Flow 165, 104475.
Machicoane, N., Ricard, G., Osuna-Orozco, R., Huck, P.D., Aliseda, A., 2020. Influence of steady and oscillating swirl on the near-field spray characteristics in a two-fluid coaxial atomizer. Int. J. Multiph. Flow (ISSN: 03019322) 129, 103318.
Machicoane, N., Volk, R., 2021. Transport of large particles through the transition to turbulence of a swirling flow. Phys. Rev. Fluids 6 (4), 044303.
Marmottant, P., Villermaux, E., 2004. On spray formation. J. Fluid Mech. 498, 73–111.
Matas, J.-P., Delon, A., Cartellier, A., 2018. Shear instability of an axisymmetric air–water coaxial jet. J. Fluid Mech. 843, 575–600.
Maxey, M.R., 1987. The motion of small spherical particles in a cellular flow field. Phys. Fluids 30 (7), 1915–1928.
Paganin, D., Mayo, S.C., Gureyev, T.E., Miller, P.R., Wilkins, S.W., 2002. Simultaneous phase and amplitude extraction from a single defocused image of a homogeneous object. J. Microscopy 206 (1), 33–40.
Powell, C.F., Yue, Y., Poola, R., Wang, J., 2000. Time-resolved measurements of supersonic fuel sprays using synchrotron X-rays. J. Synchrotron Radiat. 7 (6), 356–360.
Ricard, G., Machicoane, N., Osuna-Orozco, R., Huck, P.D., Aliseda, A., 2021. Role of convective acceleration in the interfacial instability of liquid-gas coaxial jets. Phys. Rev. Fluids 6 (8), 084302.
Singh, G., Kourmatzis, A., Gutteridge, A., Masri, A., 2020. Instability growth and fragment formation in air assisted atomization. J. Fluid Mech. 892.
Stamati, O., Marks, B., Andò, E., Roux, S., Machicoane, N., 2023. X-ray radiography 4D particle tracking of heavy spheres suspended in a turbulent jet. Int. J. Multiph. Flow 162, 104406.
Tolfts, O., 2023. Morphology, statistics, and time dynamics of the liquid jet breakup in coaxial two-fluid atomization (Ph.D. thesis). Université Grenoble Alpes.
Tolfts, O., Deplus, G., Machicoane, N., 2023. Statistics and dynamics of a liquid jet under fragmentation by a gas jet. Phys. Rev. Fluids 8 (4), 044304.
Van Kampen, N.G., 1981. Stochastic processes in physics and chemistry. Elsevier.
Villermaux, E., 2020. Fragmentation versus cohesion. J. Fluid Mech. 898, P1.
Vu, L., Machicoane, N., Li, D., Morgan, T.B., Heindel, T.J., Aliseda, A., Desjardins, O., 2023. A computational study of a two-fluid atomizing coaxial jet: Validation against experimental back-lit imaging and radiography and the influence of gas velocity and contact line model. Int. J. Multiph. Flow 167, 104520.
Wang, Y., Im, K.-S., Fezzaa, K., 2008. Similarity between the primary and secondary air-assisted liquid jet breakup mechanisms. Phys. Rev. Lett. 100 (15), 154502.
Weitkamp, T., Haas, D., Wegrzynek, D., Rack, A., 2011. Ankaphase: software for single-distance phase retrieval from inline X-ray phase-contrast radiographs. J. Synchrotron Radiat. 18 (4), 617–629.